Chemical Science

ROYAL SOCIETY OF CHEMISTRY

EDGE ARTICLE

View Article Online
View Journal | View Issue

Cite this: *Chem. Sci.*, 2023, **14**, 12238

All publication charges for this article have been paid for by the Royal Society of Chemistry

Received 18th August 2023
Accepted 14th October 2023

DOI: 10.1039/d3sc04332k

rsc.li/chemical-science

In situ recrystallization of zero-dimensional hybrid metal halide glass-ceramics toward improved scintillation performance†

Bohan Li,[a] Jiance Jin,[b] Meijuan Yin,[a] Kai Han,[b] Yuchi Zhang,[a] Xinlei Zhang,[a] Anran Zhang,[b] Zhiguo Xia*[b] and Yan Xu*[a]

Zero-dimensional (0D) hybrid metal halide (HMH) glasses are emerging luminescent materials and have gained attention due to their transparent character and ease of processing. However, the weakening of photoluminescence quantum efficiency from crystal to glass phases poses limitations for photonics applications. Here we develop high-performance glass-ceramic (G-C) scintillators *via in situ* recrystallization from 0D HMH glass counterparts composed of distinct organic cations and inorganic anions. The G-C scintillators maintain excellent transparency and exhibit nearly 10-fold higher light yields and lower detection limits than those of glassy phases. The general *in situ* recrystallization within the glass component by a facile heat treatment is analyzed *via* combined experimental elaboration and structural/spectral characterization. Our results on the development of G-Cs can initiate more exploration on the phase transformation engineering in 0D HMHs, and therefore make them highly promising for large-area scintillation screen applications.

Introduction

Zero-dimensional (0D) hybrid metal halides (HMHs) are widely used as light-emitting diodes, sensors, scintillators, *etc.* because of their excellent optical properties and good structural tunability.[1–9] Due to the unique molecular structure of 0D metal halide crystals, that is, consisting of mutually isolated inorganic anions and organic cations, the design synthesis of 0D HMH crystals with diverse structures and optical properties has been continuously pursued.[10–18] Recently, our group initially reported on the glass formation process and scintillation applications of an $(ETP)_2MnBr_4$-based transparent medium, which has sparked broader interests in 0D HMH glasses.[19] Generally, strictly manipulating the organic–inorganic components and avoiding irreversible decomposition before melting simultaneously is the key to obtaining luminescent 0D HMH glasses, which in turn leads to easy processing and high transparency.[20–23]

Vitrification is a thermally dependent phenomenon that involves the conversion of a material from a solid to a stable liquid or glassy state, which is characterized by the absence of long-range molecular order.[24–27] Only a few crystals feature a capacity to afford such stable transitions to either of these states following amorphization without compositional decomposition.[28–31] Hybrid glasses representing a relatively novel class of materials, dominated by metal–organic framework glasses, coordination polymers glasses and HMH glasses discussed herein, are capable of undergoing glass transition by connecting both organic and inorganic parts in a cooperative manner.[32–36] Unlike single-crystal materials that are challenging to grow to sufficient size, organic–inorganic hybrid glasses offer enhanced processability and moldability.[37–40] These glasses can be used as a matrix to disperse pre-prepared MOF crystals or other nanoparticles to obtain functional hybrid crystal–glass composites with improved physicochemical properties and which have been extensively studied.[41–43] However, there is still a lack of understanding on how to achieve *in situ* recrystallization from the melt within the hybrid glass matrix to obtain unique glass-ceramics (G-Cs) with outstanding and intriguing properties.[44]

Here, we have successfully designed and prepared a series of 0D HMH based glasses by modulating diverse organic cations and inorganic anions in their constituents. Flexible manufacturing of optical fibers and large-size glass wafers further demonstrates the excellent processability of these 0D HMH glasses. ^{31}P solid-state NMR and Mn K-edge EXAFS for selected Mn-based 0D HMH glass show that the tetra-coordination structure of the phosphorus and Mn luminescent center was retained after vitrification, so that the characteristic emissions are preserved. But the simple melting-process

[a]*Department of Chemistry, College of Sciences, Northeastern University, Shenyang, 110819, China. E-mail: xuyan@mail.neu.edu.cn*

[b]*State Key Laboratory of Luminescent Materials and Devices, Guangdong Provincial Key Laboratory of Fiber Laser Materials and Applied Techniques, School of Materials Science and Engineering, South China University of Technology, Guangzhou, 510641, China. E-mail: xiazg@scut.edu.cn*

† Electronic supplementary information (ESI) available. See DOI: https://doi.org/10.1039/d3sc04332k

can result in a remarkable decrease of quantum efficiency, which also inevitably occurred in previous research,[22] restricting the applications of these 0D HMH glasses. *In situ* recrystallization in the 0D HMH glass phase has great potential to address the issue although it is challenging in experiments and mechanisms. Herein we integrated the melt-processing and a stepwise heating method to obtain corresponding G-Cs, exhibiting enhanced light yield, a lower detection limit in X-ray scintillation applications, and improved imaging resolution in X-ray imaging compared to conventional glass. Therefore, this work provides a simple and feasible pre-treatment strategy to efficiently modulate the nature of 0D HMH glasses with superior scintillation performances for optical radiation detection.

Results and discussion

Six different ionic liquids were selected here as organic ligands to synthesize single crystals of $(BTP)_2MnBr_4$ (BTP = benzyltriphenylphosphonium), $(MTP)_2MnBr_4$ (MTP = methyltriphenylphosphonium), $(ETP)_2MnBr_4$ (ETP = ethyltriphenylphosphonium), $(BuTP)_2MnBr_4$ (BuTP = butyltriphenylphosphonium), $(1\text{-EP})_2MnBr_4$ (1-EP = 1-ethylpyridine) and $(1\text{-BuP})_2MnBr_4$ (1-BuP = 1-butylpyridine). Detailed crystallography data of these crystals were collected, and they are composed of different organic ligands with $(MnBr_4)^{2-}$ inorganic tetrahedra (ESI Fig. 1 and 2 and ESI Table 1†), and the as-grown crystals of these 0D HMHs can be easily melted at different temperatures. Upon melting, $(BTP)_2MnBr_4$, $(MTP)_2MnBr_4$, $(ETP)_2MnBr_4$ and $(BuTP)_2MnBr_4$ give transparent blocks, whereas $(1\text{-EP})_2MnBr_4$ and $(1\text{-BuP})_2MnBr_4$ were obtained as opaque blocks (Fig. 1a). To clearly understand this phenomenon, we monitored the temperature rise and fall process of the HMHs using differential scanning calorimetry (DSC). As the temperature increases, all six 0D HMHs melt before the decomposition temperature, but they exhibit differences during the subsequent temperature decrease (ESI Fig. 3†). When the temperature decreases, the 0D HMHs with higher melting temperature (T_m), assembling from larger quaternary phosphonium organic ligands, changed from the molten state to the amorphous state, while the 0D HMHs with lower T_m and containing smaller pyridinium organic ligands recrystallized from the molten state to the crystalline state again (ESI Fig. 4†). The transparent blocks of $(BTP)_2MnBr_4$, $(MTP)_2MnBr_4$, $(ETP)_2MnBr_4$, and $(BuTP)_2MnBr_4$ with amorphous diffraction peaks display glass transition temperatures (T_g) instead of a fixed T_m in the monitored DSC curves. This T_g ranges from 42 °C to 74 °C, commonly observed in glass samples (Fig. 1b). The appearance of the T_g indicates that $(BTP)_2MnBr_4$, $(MTP)_2MnBr_4$, $(ETP)_2MnBr_4$, and $(BuTP)_2MnBr_4$ underwent a transformation from the crystalline to glassy state after the melting and cooling process. Conversely, $(1\text{-EP})_2MnBr_4$ and $(1\text{-BuP})_2MnBr_4$ show exothermic peaks due to recrystallization during cooling, which prevents the formation of the glassy state (ESI Fig. 5†).

Besides organic cations, the physical and chemical properties of HMHs are dominantly determined by the inorganic anions in the crystal structure.[45,46] We attempted to broaden the synthetic pathway for HMH glasses to encompass various metal types of 0D HMH compounds through alterations of the inorganic anionic components. As an example, we selected an ionic liquid of ETPBr as the organic ligand to synthesize various metal ions containing 0D HMH, including Co^{2+}, Ni^{2+}, Zn^{2+} and Bi^{3+} with their corresponding crystal structures shown in ESI Fig. 6 and 7,† and the corresponding crystal data shown in ESI Table 2.† Surprisingly, pure ETPBr without the introduction of any metal ions, as well as the HMHs of $(ETP)_2CoBr_4$, $(ETP)_2NiBr_4$, $(ETP)_2ZnBr_4$, and $(ETP)_3Bi_2Br_9$ crystals can also form corresponding glass samples after melting, showing different body colors (ESI Fig. 8 and 9†). The ionic liquid of ETPBr without metal ions melts at approximately 207 °C, forming organic small molecule glass with a T_g of around 48 °C once cooled (Fig. 1c). When organic ligands are combined with different inorganic polyhedra, such as $(MnBr_4)^{2-}$, $(CoBr_4)^{2-}$, $(NiBr_4)^{2-}$, $(ZnBr_4)^{2-}$ tetrahedra and $(Bi_2Br_9)^{3-}$ dimer to form 0D HMHs, the T_m decreases compared to ETPBr and can form related hybrid glasses possessing different UV absorption spectra (ESI Fig. 10†). Monitoring of the T_g for various 0D HMH glasses revealed a correlation between the T_g and the atomic number of the metal ion. One can find that T_g increases gradually with an increase in atomic number of metal ions.

Similarly, the alteration of the halogen ions can also preserve the glass transition ability of 0D HMHs. As an example, we synthesized $(ETP)_2MnCl_4$ and successfully obtained the corresponding glass sample with a specific T_g (ESI Fig. 11 and ESI Table 3†). The successful preparation of these diverse 0D HMH glasses indicates that screening of appropriate ionic liquids is critical to achieve the glass transition of 0D HMH crystals at a low T_g. The existence of low T_g for 0D HMH glass affords it a unique ability to bend and fold near the T_g, indicating an excellent workability under mild conditions (Fig. 1d). Using this property, we prepared optical fibers with a diameter of about 400 μm, and a uniform distribution of elements was observed in the fibers using EDS (Fig. 1e and ESI Fig. 12†). Likewise, we can create glass discs that are 10 cm in diameter and have excellent light transmission properties (Fig. 1f).

The conversion of 0D HMHs from crystals to glasses can be verified by XRD patterns (Fig. 2a). To further explore the structural transformations in detail, ^{31}P solid-state nuclear magnetic resonance (NMR) and extended X-ray absorption fine structure (EXAFS) techniques were employed to investigate the coordination modes of P and Mn ions in the selected 0D HMH of $(BTP)_2MnBr_4$ as an example. Fig. 2b illustrates that the peak positions of ^{31}P spectra for the $(BTP)_2MnBr_4$ glass sample align perfectly with those of the crystal, unequivocally confirming the retention of the four-coordinated P atom in $(BTP)_2MnBr_4$.[47] To examine the phase transformation of $(MnBr_4)^{2-}$ tetrahedra during crystalline–glass transition of $(BTP)_2MnBr_4$, we recorded the Mn K-edge EXAFS data of $(BTP)_2MnBr_4$ glass and crystal (ESI Fig. 13†), respectively. The Fourier transforms of the Mn K-edge EXAFS spectra of $(BTP)_2MnBr_4$ glass and crystal are similar, exhibiting two peaks at 1.5 Å and 2.2 Å, which can be attributed to the Mn–Br bond (Fig. 2c). The Mn–Br bond lengths in the $(BTP)_2MnBr_4$ glass were fitted to be approximately 2.53 Å and 2.63 Å, which are comparable to those of the $(BTP)_2MnBr_4$ crystal (Fig. 2d and ESI Table 4†).[48] The near-identical Mn K-

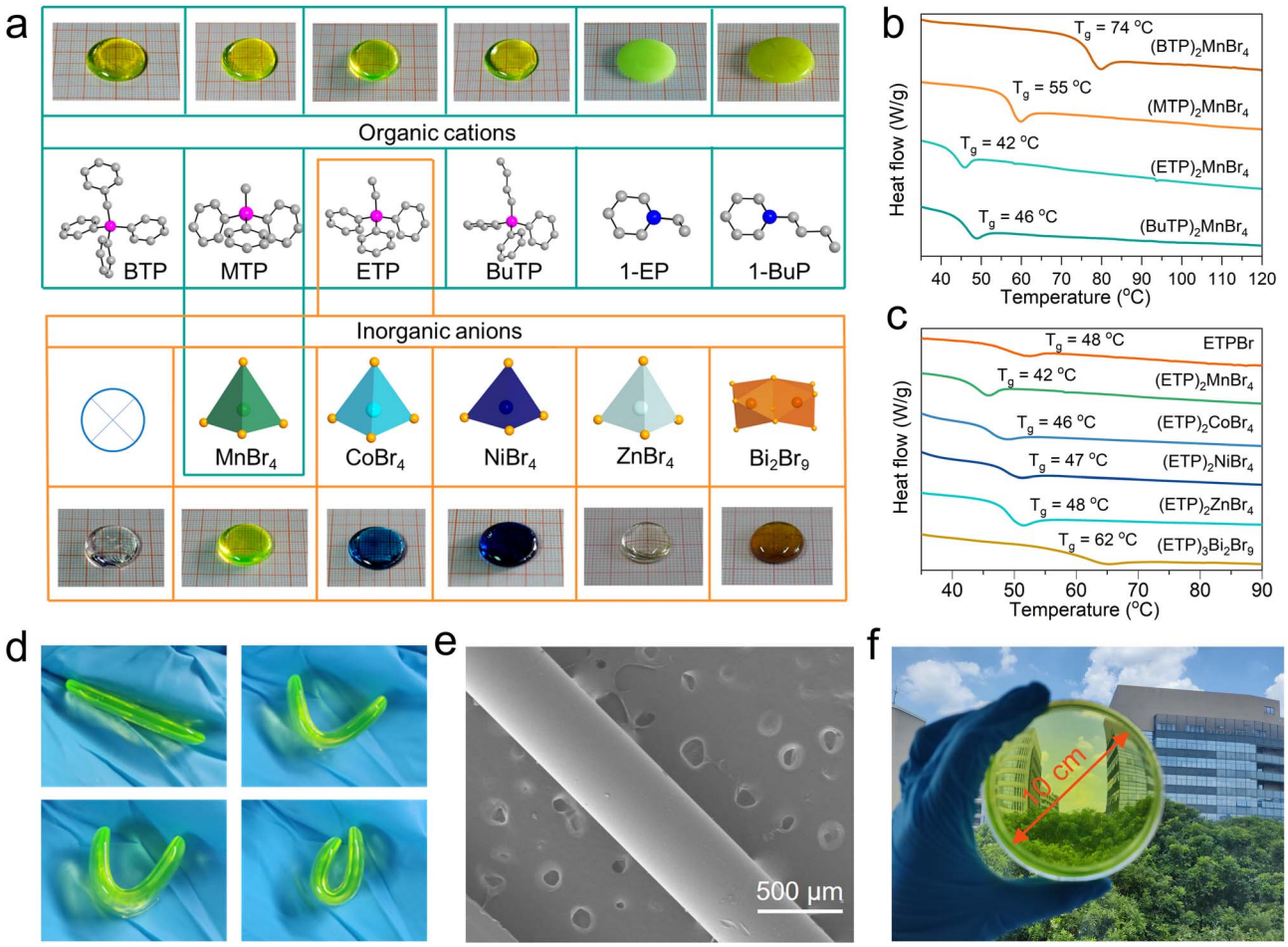

Fig. 1 (a) Schematic diagrams of the different 0D HMH melt products obtained by modulating the organic and inorganic components. Pink sphere, P; blue, N; gray, C; green, Mn; orange, Br; light blue, Co; white, Zn, orange-red, Bi; dark blue, Ni. (b) DSC up-scans for $(BTP)_2MnBr_4$, $(MTP)_2MnBr_4$, $(ETP)_2MnBr_4$, and $(BuTP)_2MnBr_4$ glasses. (c) DSC up-scans for ETPBr, $(ETP)_2MnBr_4$, $(ETP)_2CoBr_4$, $(ETP)_2NiBr_4$, $(ETP)_2ZnBr_4$ and $(ETP)_3Bi_2Br_9$ glasses. (d) Optical images of glass samples at different bending levels. (e) SEM picture of glass fibers. (f) The glass wafer with a diameter of 10 cm, captured at 298 K.

edge EXAFS curves of the $(BTP)_2MnBr_4$ glass and crystal confirm the complete preservation of the $(MnBr_4)^{2-}$ tetrahedral component within the glass structure upon vitrification.[49] Likewise, the similarity of glass and crystal phases in IR spectra and Raman spectra further demonstrate the retention of organic and inorganic components in the glass (ESI Fig. 14 and 15†).[50,51] In considering the analysis results of XRD, ^{31}P solid NMR, EXAFS, IR spectra, and Raman spectra of $(BTP)_2MnBr_4$ glass and crystal, we can conclusively describe the structure transition of $(BTP)_2MnBr_4$. When the $(BTP)_2MnBr_4$ crystals vitrify to glass, the regularly arranged crystal structure changed into a disordered glass structure, but the organic cations and the $(MnBr_4)^{2-}$ tetrahedra in the crystal were preserved in the glass phase, supported by ^{31}P solid NMR and Mn K-edge EXAFS (Fig. 2e and f) as discussed above.

Due to the retention of the tetra-coordinated structure of Mn^{2+} in $(BTP)_2MnBr_4$ glass, its fluorescence emission and decay lifetime are similar to that of the crystal (ESI Fig. 16 and 17†). During the crystal–glass transition, the quantum efficiency and scintillation performance of the glass decreases, making the glass sample substantially less promising for optical functional applications (ESI Fig. 18 and ESI Table 5†). Intriguingly, the DSC curve of $(BTP)_2MnBr_4$ glass shows an exothermic peak at about 130 °C higher than T_g, indicating the recrystallization of the glass during a stepwise temperature heating (Fig. 3a). This result was further confirmed by temperature-dependent XRD characterization, proving the *in situ* transformation of the amorphous $(BTP)_2MnBr_4$ glass into its crystalline phase again upon heating (Fig. 3b). Although the exothermic peak of crystallization was not monitored on the DSC curves of the other 0D HMH glasses, all of them could afford the *in situ* crystallization of 0D HMH glass by heat treatment. The XRD of the 0D HMH glasses after heat treatment at different temperatures indicated that this phenomenon is general in 0D HMH glasses (ESI Fig. 19†).

By holding the glass samples at 130–150 °C, we achieved *in situ* recrystallization inside the glass, resulting in $(BTP)_2MnBr_4$ G-C. Fig. 3c shows that the smooth surface of the glass changed into stacked microcrystals with a grain size of about 1 μm. After recrystallization at 130 °C, the transmittance of the glass is

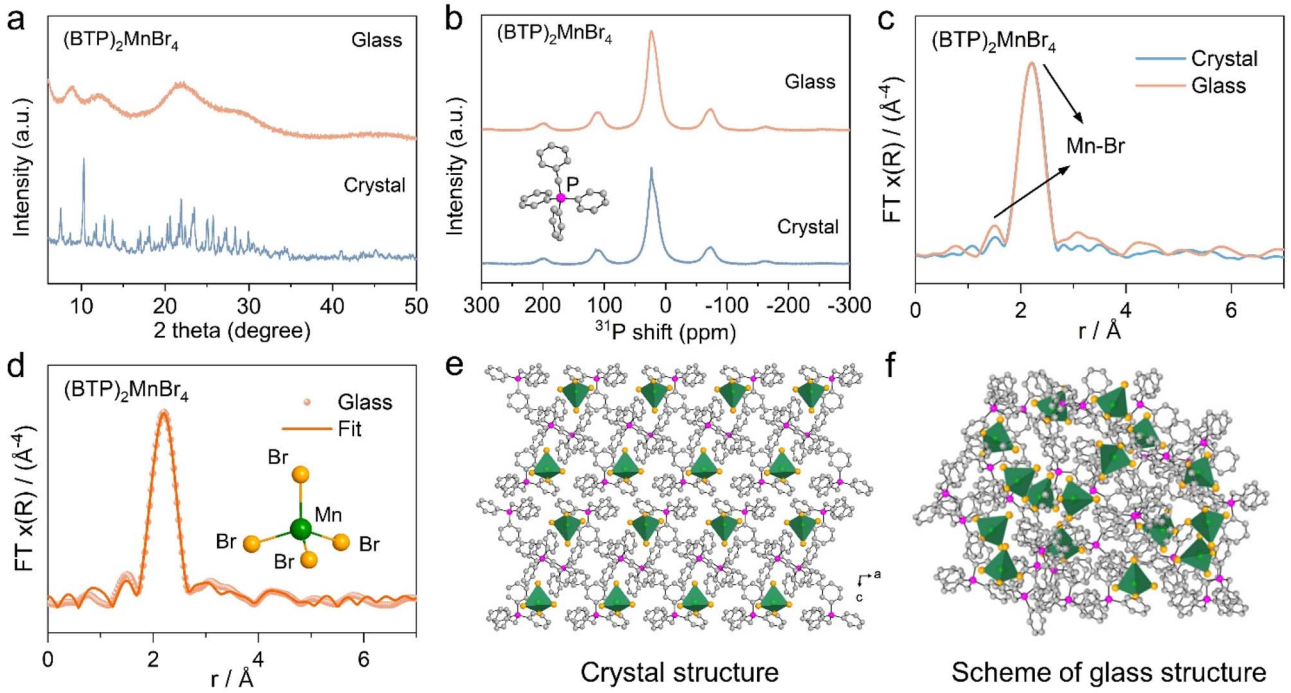

Fig. 2 (a) PXRD patterns of the $(BTP)_2MnBr_4$ crystal and glass. (b) ^{31}P solid-state NMR patterns of the $(BTP)_2MnBr_4$ crystal and glass. (c) Measured Fourier-transformed Mn K-edge EXAFS spectra of the $(BTP)_2MnBr_4$ crystal and glass. (d) Fitting of the EXAFS of $(BTP)_2MnBr_4$ glass confirmed a four-connected Mn(II) node. (e and f) Schematic diagrams of the crystal (e) and glass (f) structure of $(BTP)_2MnBr_4$ as an example.

greatly preserved, and the as-formed G-C still has 60% transmittance between 500 and 1500 nm (Fig. 4a). As the recrystallization temperature increases, the grain size increases and the sample transmittance decreases (ESI Fig. 20 and 21†). By comparing the light yield with that of the standard scintillator LuAG:Ce, the G-C demonstrated a nearly 10-fold improvement over the glass sample, achieving an excellent light yield of 85 500 ph MeV^{-1} (Fig. 4b and ESI Fig. 22†). Furthermore, the $(BTP)_2MnBr_4$ G-C exhibited a lower detection limit than the glass sample, with a detection limit of 43.4 nGy s^{-1}, well below

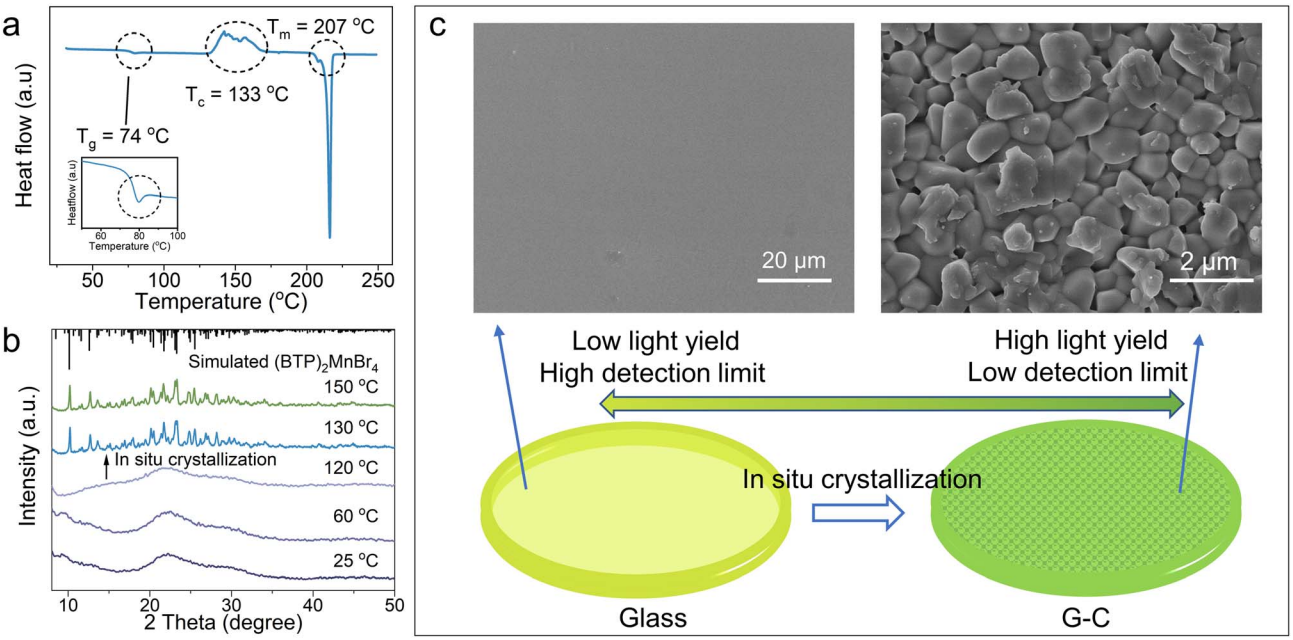

Fig. 3 (a) DSC curve of $(BTP)_2MnBr_4$ glass. (b) Variable temperature-dependent PXRD patterns of $(BTP)_2MnBr_4$ glass. (c) Demonstration of *in situ* recrystallization of HMH glasses and SEM images of glass and post-recrystallization G-C.

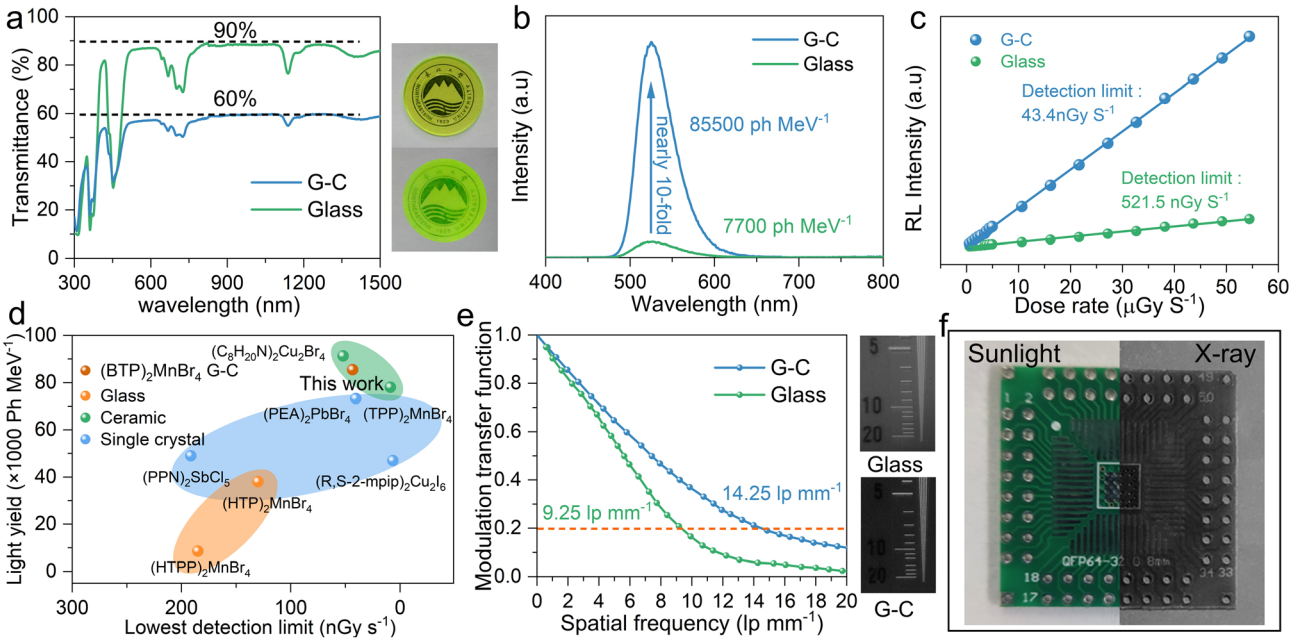

Fig. 4 (a) Light transmittance of $(BTP)_2MnBr_4$ glass and G-C (inset shows photographs of $(BTP)_2MnBr_4$ glass and G-C). (b) X-ray radio luminescence (RL) spectra of $(BTP)_2MnBr_4$ glass and G-C under X-ray irradiation. (c) Linear relationship between the dose rate and RL intensity for $(BTP)_2MnBr_4$ glass and G-C scintillator. (d) Comparison of light yield and detection limits of different scintillation blocks. (e) Modulation transfer functions (MTF) of X-ray images obtained from $(BTP)_2MnBr_4$ glass and G-C. (f) Photograph and X-ray image of a 4 cm diameter circuit board.

the required metering rate for X-ray diagnostics (5.5 μGy s^{-1}), significantly reducing the radiation dose required for use in medical examinations (Fig. 4c). When compared to other high-performance bulk hybrid scintillation materials, the large-area $(BTP)_2MnBr_4$ G-C *via* such a recrystallization processing technique demonstrates a higher yield and lower detection limit than those of scintillation glass, placing it on par with scintillation ceramics and single crystals (Fig. 4d).[5,22,23,52–55]

To demonstrate the practical application of the as-obtained HMH G-Cs as scintillators in X-ray imaging, we compared the spatial resolution of $(BTP)_2MnBr_4$ G-C to that of glass samples. The $(BTP)_2MnBr_4$ G-C exhibited excellent spatial resolution (14.25 lp mm^{-1}), surpassing obviously that of the $(BTP)_2MnBr_4$ glass (9.25 lp mm^{-1}) due to the outstanding transmittance and high light yield (Fig. 4e). Images of the X-ray standard resolution test template provide further evidence of the superior spatial resolution achieved by $(BTP)_2MnBr_4$ G-C (ESI Fig. 23†). Subsequent imaging experiments demonstrated the practicality of $(BTP)_2MnBr_4$ G-C in X-ray imaging applications. Clear circuit structures and the fine needles inserted into a chicken that were not visible under fluorescent light could be successfully captured under X-ray irradiation (Fig. 4f and ESI Fig. 24†).

Conclusions

In summary, we have developed a general *in situ* recrystallization process within the 0D HMH glass components to prepare high-performance glass-ceramics. Four quaternary phosphonium ionic liquids can be amorphized in combination with $(MnBr_4)^{2-}$ to form 0D HMH glasses with very low T_g and good processing properties. By utilizing ethyltriphenylphosphonium (ETP) with vitrification capability as organic cations, the luminescent center in 0D HMH glasses can be expanded to diverse polyhedra composed of different metal and halogen ions. ^{31}P solid-state NMR and EXAFS tests support that the 0D HMH glass retains the coordination environment of organic cations and inorganic polyhedra of HMH crystals after vitrification, but the photoluminescence quantum efficiency and scintillation performance are reduced. By applying an *in situ* recrystallization strategy through holding the glass phase at 130 °C, the G-Cs originating from 0D HMH glass were successfully generated, showing 10-fold light yield and reduced detection limit in comparison to the glass phase as scintillators. The excellent transmittance and greatly improved scintillation performance of large-area G-Cs make them great candidates for X-ray imaging applications. The concept of exploiting recrystallization of 0D HMH glass toward G-Cs is expected to open the gateway for developing high performance scintillators, and allow them to become an emerging optical functional material.

Experimental section

Synthesis. Growth of $(BTP)_2MnBr_4$, $(MTP)_2MnBr_4$, $(ETP)_2MnBr_4$, $(BuTP)_2MnBr_4$, $(1\text{-}EP)_2MnBr_4$ and $(1\text{-}BuP)_2MnBr_4$ single crystals

Specifically, BTPBr (1 mmol), MTPBr (1 mmol), ETPBr (1 mmol), BuTPBr (1 mmol), 1-EPBr (1 mmol) or 1-BuP (1 mmol) and $MnBr_2$ (0.5 mmol) were dissolved in ethanol under stirring conditions. Then, crystals of $(BTP)_2MnBr_4$, $(MTP)_2MnBr_4$, $(ETP)_2MnBr_4$, $(BuTP)_2MnBr_4$, $(1\text{-}EP)_2MnBr_4$ and $(1\text{-}BuP)_2MnBr_4$

were gradually precipitated with the volatilization of ethanol, and the crystals were collected.[56]

Growth of $(ETP)_2CoBr_4$, $(ETP)_2NiBr_4$, $(ETP)_2ZnBr_4$ and $(ETP)_3Bi_2Br_9$ single crystals

Specifically, ETPBr (1 mmol) and $CoBr_2$ (0.5 mmol), $NiBr_2$ (0.5 mmol), $ZnBr_2$ (0.5 mmol) or $BiBr_3$ (0.66 mmol) were dissolved in dichloromethane (99.9%, 2 mL) under stirring conditions. Then, the counter-solvent ether was added and left for one to two days, and the crystals of $(ETP)_2CoBr_4$, $(ETP)_2NiBr_4$, $(ETP)_2ZnBr_4$ and $(ETP)_3Bi_2Br_9$ were gradually precipitated and collected.

Fabrication of hybrid metal halide (HMH) glass

The HMH glass was obtained by heating HMH crystal at 130–250 °C under air conditions, and cooling the melt to room temperature.

Fabrication of $(BTP)_2MnBr_4$ glass-ceramic (G-C)

The pre-prepared $(BTP)_2MnBr_4$ glass precursor was kept in an air atmosphere at 130–150 °C for 30 min, and the sample was removed after natural cooling, and the obtained sample was ground and polished to obtain $(BTP)_2MnBr_4$ G-C.

Characterization

The single crystal data was collected using the XtaLAB AFC12 X-ray four-circle single crystal diffractometer (Rigaku) equipped with a CCD-detector, graphite monochromator and Cu Kα radiation source. Powder X-ray diffraction (PXRD) patterns and the variable temperature-dependent PXRD measurements were taken on an Aeris PXRD diffractometer (PANalytical Corporation, the Netherlands) operating at 40 kV and 15 mA with monochromatized Cu Kα radiation (λ = 1.5406 Å). Variable temperature-dependent PXRD was conducted from room temperature to 150 °C with a heating rate of 10 °C min^{-1} and data was collected after holding at 25 °C, 60 °C, 120 °C, 130 °C, and 150 °C for 10 minutes. The photoluminescence excitation (PLE), photoluminescence (PL) and PL decay spectra measurements were performed on an FLS1000 fluorescence spectrophotometer (Edinburgh Instruments Ltd., UK). The photoluminescence quantum yields were recorded using a Hamamatsu Quantaurus-QY spectrometer (model C11347-11). The PLQYs were calculated based on the equation: $\eta_{QE} = I_S/(E_R - E_S)$, in which I_S denotes the luminescence emission spectral area of the sample, E_R is the excitation light spectral area of the null integrating sphere, and E_S is the excitation light spectral area of the excited sample. Differential scanning calorimetry (DSC) measurements were carried out on a TA DSC Q2000 mainly focusing on its thermotropic behavior. The sample was heated at a scan rate of 5 °C min^{-1}. After cooling to room temperature, the second up-scan was performed using the same procedure as the first scan. Thermogravimetric analysis (TGA) was conducted on a TG 209F3 from 30 to 500 °C in an argon atmosphere with a ramping rate of 10 °C min^{-1}. The light transmittance spectra were recorded using a Lambda 750 spectrophotometer (PerkinElmer, USA) in the range from 300 to 1500 nm. Raman data was collected on an XploRA PLUS (λ = 785 nm). Fourier-transform infrared (FTIR) was performed on a Bruker VERTEX 70. A solid state NMR experiment was carried out on a Bruker 600 MHz (14.1 T) magnet with AVANCE NEO consoles using a Bruker 3.2 mm HXY magic angle spinning (MAS) probe. The Larmor frequency for ^{31}P was determined to be 242.99 MHz. ^{31}P spectra were acquired with one pulse and referenced to 85% H_3PO_4 solution (0 ppm). The Mn K-edge extended X-ray absorption fine structure (EXAFS) spectra were collected at beamline BL14W1 of SSRF operated at 3.5 GeV in "top-up" mode with a constant current of 220 mA. The energy was calibrated according to the absorption edge of pure Mn foil. EXAFS data from the solid samples were recorded in transmission mode with high-flux ion chambers with a 32-element Ge solid-state detector, respectively. The duration of the measurement was about 0.5 h for each sample. The extended XAFS (EXAFS) data were analyzed using the DEMETER software package.[40] Radioluminescence spectra at room temperature (RT) were recorded using an FLS1000 fluorescence spectrophotometer (Edinburgh Instruments Ltd., Edinburgh, U.K.). The $(BTP)_2MnBr_4$ glass, G-C and the commercial scintillator LuAG:Ce were tightly attached to the circular window of an integrating sphere with an X-ray source (Amptek Mini-X tube with a Mo target and a maximum power output of 6 W). The LY values can be calculated from the total ratio of the number of emitted photons for $(BTP)_2MnBr_4$ glass, G-C and the commercial scintillator LuAG:Ce at the equivalent absorbed X-ray energy. X-ray detection limits were calculated from the linear relationship between the RL intensity and the X-ray dose of the corresponding samples. Noise data were obtained in the absence of samples. The detection limit of the corresponding sample was obtained when the signal-to-noise ratio was 3. X-ray imaging was acquired by using a complementary metal oxide semiconductor camera. MTF measurements can be used to evaluate the fundamental spatial resolution performance of an imaging system. The spatial resolution can be determined by the spatial frequency value when MTF = 0.2. The MTF curve was calculated by the slanted-edge method.

Data availability

All data needed to evaluate the conclusions are present in the paper and ESI.† The data that support the findings of this study are available from the corresponding author upon request.

Author contributions

Y. X. and Z. G. X. initiated and guided the research. B. H. L. synthesized the samples and wrote the manuscript, and Y. X. and Z. G. X. revised it. B. H. L., J. C. J., M. J. Y., K. H. and X. L. Z. interpreted the theoretical and experimental results. Y. C. Z. and A. R. Z. performed the morphological and structural characterization. All authors discussed the results and commented on the manuscript.

Conflicts of interest

There are no conflicts to declare.

Acknowledgements

This work was supported by the National Natural Science Foundation of China (Grant No. 22171040), the Fundamental Research Funds for the Central Universities, China (No. N2105006), and the Guangdong Provincial Science & Technology Project (2023A0505050084).

References

1 M. Li and Z. Xia, *Chem. Soc. Rev.*, 2021, **50**, 2626–2662.
2 S. Sun, M. Lu, X. Gao, Z. Shi, X. Bai, W. W. Yu and Y. Zhang, *Adv. Sci.*, 2021, **8**, 2102689.
3 P. Tao, S. J. Liu and W. Y. Wong, *Adv. Opt. Mater.*, 2020, **8**, 2000985.
4 L. J. Xu, X. Lin, Q. He, M. Worku and B. Ma, *Nat. Commun.*, 2020, **11**, 4329.
5 K. Han, K. Sakhatskyi, J. Jin, Q. Zhang, M. V. Kovalenko and Z. Xia, *Adv. Mater.*, 2022, **34**, 2110420.
6 T. M. Guo, Y. J. Gong, Z. G. Li, Y. M. Liu, W. Li, Z. Y. Li and X. H. Bu, *Small*, 2022, **18**, 2103829.
7 P. K. Rajput, A. K. Poonia, S. Mukherjee, T. Sheikh, M. Shrivastava, K. V. Adarsh and A. Nag, *J. Phys. Chem. C*, 2022, **126**, 9889–9897.
8 H. Wang, J. X. Wang, X. Song, T. He, Y. Zhou, O. Shekhah, L. Gutierrez-Arzaluz, M. Bayindir, M. Eddaoudi, O. M. Bakr and O. F. Mohammed, *ACS Cent. Sci.*, 2023, **9**, 668–674.
9 R. W. Huang, X. Song, S. Chen, J. Yin, P. Maity, J. Wang, B. Shao, H. Zhu, C. Dong, P. Yuan, T. Ahmad, O. F. Mohammed and O. M. Bakr, *J. Am. Chem. Soc.*, 2023, **145**, 13816–13827.
10 M. Li, J. Zhou, G. Zhou, M. S. Molokeev, J. Zhao, V. Morad, M. V. Kovalenko and Z. Xia, *Angew. Chem., Int. Ed.*, 2019, **58**, 18670–18675.
11 L. J. Xu, A. Plaviak, X. Lin, M. Worku, Q. He, M. Chaaban, B. J. Kim and B. Ma, *Angew. Chem., Int. Ed.*, 2020, **59**, 23067–23071.
12 Q. Li, B. Xu, Z. Chen, J. Han, L. Tan, Z. Luo, P. Shen and Z. Quan, *Adv. Funct. Mater.*, 2021, **31**, 2104923.
13 B. Su, S. Geng, Z. Xiao and Z. Xia, *Angew. Chem., Int. Ed.*, 2022, **61**, e202208881.
14 T. Huang, Q. Wei, W. Lin, H. Peng, S. Yao and B. Zou, *Mater. Today Phys.*, 2022, **25**, 100703.
15 J. Lu, J. Gao, S. Wang, M. J. Xie, B. Y. Li, W. F. Wang, J. R. Mi, F. K. Zheng and G. C. Guo, *Nano Lett.*, 2023, **23**, 4351–4358.
16 A. S. Kshirsagar, H. Arfin, S. Banerjee, B. Mondal and A. Nag, *J. Phys. Chem. C*, 2021, **125**, 27671–27677.
17 H. Meng, B. Chen, W. Zhu, Z. Zhou, T. Jiang, X. Xu, S. Liu and Q. Zhao, *Laser Photonics Rev.*, 2023, **17**, 2201007.
18 D. Y. Li, J. H. Song, Z. Y. Xu, Y. J. Gao, X. Yin, Y. H. Hou, L. J. Feng, C. Y. Yue, H. Fei and X. W. Lei, *Chem. Mater.*, 2022, **34**, 6985–6995.
19 B. Li, Y. Xu, X. Zhang, K. Han, J. Jin and Z. Xia, *Adv. Opt. Mater.*, 2022, **10**, 2102793.
20 Y. Zhang, Y. Zhang, Y. Zhao, H. Jia, Z. Yang, B. Yin, Y. Wu, Y. Yi, C. Zhang and J. Yao, *J. Am. Chem. Soc.*, 2023, **145**, 12360–12369.
21 B. Li, J. Jin, M. Yin, X. Zhang, M. S. Molokeev, Z. Xia and Y. Xu, *Angew. Chem., Int. Ed.*, 2022, **61**, e202212741.
22 J. B. Luo, J. H. Wei, Z. Z. Zhang, Z. L. He and D. B. Kuang, *Angew. Chem., Int. Ed.*, 2023, **62**, e202216504.
23 Y. Xu, Z. Li, G. Peng, F. Qiu, Z. Li, Y. Lei, Y. Deng, H. Wang, Z. Liu and Z. Jin, *Adv. Opt. Mater.*, 2023, **11**, 2300216.
24 K. Ito, C. T. Moynihan and C. A. Angell, *Nature*, 1999, **398**, 492–495.
25 N. Ma and S. Horike, *Chem. Rev.*, 2022, **122**, 4163–4203.
26 S. Horike, S. S. Nagarkar, T. Ogawa and S. Kitagawa, *Angew. Chem., Int. Ed.*, 2020, **59**, 6652–6664.
27 C. Ye, L. N. McHugh, C. Chen, S. E. Dutton and T. D. Bennett, *Angew. Chem., Int. Ed.*, 2023, e202302406.
28 T. D. Bennett and S. Horike, *Nat. Rev. Mater.*, 2018, **3**, 431–440.
29 M. A. Ali, W. M. W. Winters, M. A. Mohamed, D. Tan, G. Zheng, R. S. K. Madsen, O. V. Magdysyuk, M. Diaz-Lopez, B. Cai, N. Gong, Y. Xu, I. Hung, Z. Gan, S. Sen, H. T. Sun, T. D. Bennett, X. Liu, Y. Yue and J. Qiu, *Angew. Chem., Int. Ed.*, 2023, **62**, e202218094.
30 G. Du, S. Wen, J. Zhao, P. Ran, D. Wang, L. Wei, X. Qiao, Y. Yang, J. Qiu and S. Zhou, *Adv. Mater.*, 2023, **35**, e2205578.
31 T. Li, W. A. Dunlap-Shohl, E. W. Reinheimer, P. Le Magueres and D. B. Mitzi, *Chem. Sci.*, 2019, **10**, 1168–1175.
32 J. Hou, M. L. Rios Gomez, A. Krajnc, A. McCaul, S. Li, A. M. Bumstead, A. F. Sapnik, Z. Deng, R. Lin, P. A. Chater, D. S. Keeble, D. A. Keen, D. Appadoo, B. Chan, V. Chen, G. Mali and T. D. Bennett, *J. Am. Chem. Soc.*, 2020, **142**, 3880–3890.
33 T. D. Bennett, Y. Yue, P. Li, A. Qiao, H. Tao, N. G. Greaves, T. Richards, G. I. Lampronti, S. A. Redfern, F. Blanc, O. K. Farha, J. T. Hupp, A. K. Cheetham and D. A. Keen, *J. Am. Chem. Soc.*, 2016, **138**, 3484–3492.
34 Z. Yin, Y. Zhao, S. Wan, J. Yang, Z. Shi, S. X. Peng, M. Z. Chen, T. Y. Xie, T. W. Zeng, O. Yamamuro, M. Nirei, H. Akiba, Y. B. Zhang, H. B. Yu and M. H. Zeng, *J. Am. Chem. Soc.*, 2022, **144**, 13021–13025.
35 R. S. K. Madsen, A. Qiao, J. Sen, I. Hung, K. Chen, Z. Gan, S. Sen and Y. Yue, *Science*, 2020, **367**, 1473–1476.
36 Z. Fan, C. Das, A. Demessence, R. Zheng, S. Tanabe, Y. S. Wei and S. Horike, *Chem. Sci.*, 2022, **13**, 3281–3287.
37 V. Nozari, O. Smirnova, J. M. Tuffnell, A. Knebel, T. D. Bennett and L. Wondraczek, *Adv. Mater. Technol.*, 2022, **7**, 2200343.
38 M. A. Ali, X. Liu, H.-T. Sun, J. Ren and J. Qiu, *Chem. Mater.*, 2022, **34**, 2476–2483.
39 R. Lin, X. Li, A. Krajnc, Z. Li, M. Li, W. Wang, L. Zhuang, S. Smart, Z. Zhu, D. Appadoo, J. Harmer, Z. Wang, A. G. Buzanich, S. Beyer, L. Wang, G. Mali, T. D. Bennett, V. Chen and J. Hou, *Angew. Chem., Int. Ed.*, 2022, **61**, e202112880.

40 S. Li, R. Limbach, L. Longley, A. A. Shirzadi, J. C. Walmsley, D. N. Johnstone, P. A. Midgley, L. Wondraczek and T. D. Bennett, *J. Am. Chem. Soc.*, 2019, **141**, 1027–1034.
41 R. Lin, M. Chai, Y. Zhou, V. Chen, T. D. Bennett and J. Hou, *Chem. Soc. Rev.*, 2023, **52**, 4149–4172.
42 J. Hou, C. W. Ashling, S. M. Collins, A. Krajnc, C. Zhou, L. Longley, D. N. Johnstone, P. A. Chater, S. Li, M. V. Coulet, P. L. Llewellyn, F. X. Coudert, D. A. Keen, P. A. Midgley, G. Mali, V. Chen and T. D. Bennett, *Nat. Commun.*, 2019, **10**, 2580.
43 C. W. Ashling, D. N. Johnstone, R. N. Widmer, J. Hou, S. M. Collins, A. F. Sapnik, A. M. Bumstead, P. A. Midgley, P. A. Chater, D. A. Keen and T. D. Bennett, *J. Am. Chem. Soc.*, 2019, **141**, 15641–15648.
44 D. X. Liu, H. L. Zhu, W. X. Zhang and X. M. Chen, *Angew. Chem., Int. Ed.*, 2023, **62**, e202218902.
45 M. Li, M. S. Molokeev, J. Zhao and Z. Xia, *Adv. Opt. Mater.*, 2020, **8**, 1902114.
46 A. N. Usoltsev, T. S. Sukhikh, A. S. Novikov, V. R. Shayapov, D. P. Pishchur, I. V. Korolkov, I. F. Sakhapov, V. P. Fedin, M. N. Sokolov and S. A. Adonin, *Inorg. Chem.*, 2021, **60**, 2797–2804.
47 J. D. Lewis, M. Ha, H. Luo, A. Faucher, V. K. Michaelis and Y. Román-Leshkov, *ACS Catal.*, 2018, **8**, 3076–3086.
48 B. Ravel and M. Newville, *J. Synchrotron Radiat.*, 2005, **12**, 537–541.
49 S. Shimono, M. Sekine, Y. Niwa, H. Sagayama, K. Araki, Y. Hata and H. Kishimura, *Mater. Res. Bull.*, 2023, **159**, 112103.
50 A. Qiao, T. D. Bennett, H. Tao, A. Krajnc, G. Mali, C. M. Doherty, A. W. Thornton, J. C. Mauro, G. N. Greaves and Y. Yue, *Sci. Adv.*, 2018, **4**, eaao6827.
51 T. D. Bennett, J. C. Tan, Y. Yue, E. Baxter, C. Ducati, N. J. Terrill, H. H. Yeung, Z. Zhou, W. Chen, S. Henke, A. K. Cheetham and G. N. Greaves, *Nat. Commun.*, 2015, **6**, 8079.
52 B. Jia, D. Chu, N. Li, Y. Zhang, Z. Yang, Y. Hu, Z. Zhao, J. Feng, X. Ren, H. Zhang, G. Zhao, H. Sun, N. Yuan, J. Ding, Y. Liu and S. F. Liu, *ACS Energy Lett.*, 2022, **8**, 590–599.
53 Z. Song, Z. Jia, X. Guo, B. Yu, G. Liu, L. Meng, Y. Liu, Q. Lin and Y. Dang, *Adv. Opt. Mater.*, 2023, **11**, 2203014.
54 Q. He, C. Zhou, L. Xu, S. Lee, X. Lin, J. Neu, M. Worku, M. Chaaban and B. Ma, *ACS Mater. Lett.*, 2020, **2**, 633–638.
55 B. Su, J. Jin, K. Han and Z. Xia, *Adv. Funct. Mater.*, 2023, **33**, 2210735.
56 Y.-Y. Ma, Y.-R. Song, W.-J. Xu, Q.-Q. Zhong, H.-Q. Fu, X.-L. Liu, C.-Y. Yue and X.-W. Lei, *J. Mater. Chem. C*, 2021, **9**, 9952–9961.